Learning Geometrically Consistent Mesh Corrections

Ștefan Săftescu and Paul Newman
Mobile Robotics Group, Oxford Robotics Institute, University of Oxford, U.K.
{stefan, pnewman}@robots.ox.ac.uk

Keywords: 3D Reconstruction, Depth Refinement, Deep Learning.

Abstract: Building good 3D maps is a challenging and expensive task, which requires high-quality sensors and careful, time-consuming scanning. We seek to reduce the cost of building good reconstructions by correcting views of existing low-quality ones in a post-hoc fashion using learnt priors over surfaces and appearance. We train a convolutional neural network model to predict the difference in inverse-depth from varying viewpoints of two meshes – one of low quality that we wish to correct, and one of high-quality that we use as a reference.
In contrast to previous work, we pay attention to the problem of excessive smoothing in corrected meshes. We address this with a suitable network architecture, and introduce a loss-weighting mechanism that emphasises edges in the prediction. Furthermore, smooth predictions result in geometrical inconsistencies. To deal with this issue, we present a loss function which penalises re-projection differences that are not due to occlusions. Our model reduces gross errors by 45.3%–77.5%, up to five times more than previous work.

1 INTRODUCTION

Dense 3D maps are a crucial component in many systems and better maps make robots easier to build and safer to operate. Despite recent progress in hardware such as the wide availability of GPUs, and algorithms that scale with the amount of data and the available hardware, high-quality maps, especially at large scales and outdoors, remain difficult to build cheaply, often requiring expensive sensors such as 3D lidars, and careful, dense scans.

The main motivation of our work is to reduce the cost of building good dense 3D maps. The reduction in cost can come from either: a) cheaper but nosier sensors, such as stereo cameras; b) less data, and therefore less time spent densely scanning an area. There are two ways in which we can produce better reconstructions with cheaper data. We can learn the kinds of errors a certain modality produces. For a stereo camera, for example, there will be missing data in areas without a lot of texture (walls, roads), and the ambiguity in depth is usually along the viewing rays. In addition, we can learn priors for a target environment: cars usually have known shapes, roads and buildings do not have holes in them, surfaces tend to be vertical or horizontal in an urban environment, etc.

We tackle the problem of correcting dense reconstructions with a convolutional neural network (CNN) that operates on rasterised views of a 3D mesh as a post-processing step, following a classical reconstruc-

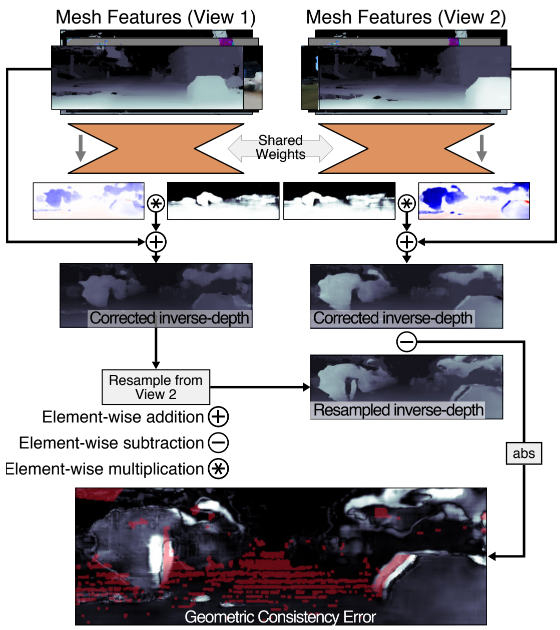

Figure 1: Illustration of geometric consistency for two views of the same scene a few meters apart. The predictions of our model can be used to compute corrected depth maps for a set of views. The corrected depth-maps should be consistent: they should be describing the same scene. To enforce this, we densely reproject inverse-depth from View 1 to View 2, using the corrected depth of View 2. The absolute difference (bottom) is the inconsistency of View 1 with respect to View 2. This is minimised during the training of our model, which enforces geometrically consistent predictions. The red overlay is the occlusion mask.

tion pipeline. To train this model, we start with two meshes, a low-quality one and a reference high-quality one. From each reconstruction, we render multiple types of images (such as inverse-depth, normals, etc.), referred to as *mesh features*, from multiple viewpoints. We then train the model on the mesh features to predict the difference in inverse-depth between the high-quality reconstruction and the low-quality one, thus enabling us to correct the low-quality mesh.

Previous work (Tanner et al., 2018) has demonstrated the idea of correcting meshes post-hoc via 2D rasterised views. We address its two main limitations. Firstly, we deal with the issue of overly smooth predictions. We propose changes to the architecture and training more suitable for our task: we add skip connections from the encoder to the decoder in our CNN, which are known to help in localising edges in predictions; we propose a loss-weighting method that penalises incorrect predictions more the closer they are to an edge. Secondly, predictions on nearby views are not always consistent, i.e. when applying the predicted corrections the geometry of the scene is not always the same. To improve consistency, we employ a view synthesis based loss, and show that this also improves the performance of the network. An illustration of the geometric consistency loss is shown in Figure 1, while Figure 2 shows an overview of our method.

Our contributions are as follows:

Error correction: We propose a CNN model that is able to correct 2D views of a dense 3D reconstruction. We propose a novel weighting mechanism to improve performance around edges in the prediction. We evaluate it against existing work and show that we outperform it, especially when images are from multiple viewpoints.

Geometric consistency: We adapt the photometric consistency loss that features in related tasks such as depth-from-mono (Godard et al., 2017) to the task of correcting reconstructions. This is a novel use of the loss, which has thus far only been employed on RGB images. We leverage the existing reconstruction to compute occlusion masks, and thus exclude from the loss areas where geometric consistency is impossible. We show that this use of geometric consistency as an auxiliary loss further improves our model.

2 RELATED WORK

Several systems for building 3D reconstructions have been proposed, such as BOR^{2}G (Tanner et al., 2015) or KinectFusion (Newcombe et al., 2011). Our approach is to correct the *output* of such a system by looking at the meshes it builds. As we operate on inverse-depth images, our work is similar to depth refinement. Below, we review some of the literature on that topic, as well as some other methods that our system draws inspiration from.

Filtering and Optimisation of Depth

Improving depth or disparity images is a well-researched area, with various methods proposed, some of which are guided by an additional aligned colour image. The most straightforward unguided techniques are based on minimising either on a joint bilateral filter (JBF) (Tomasi and Manduchi, 1998) when filtering, or Total Generalised Variation (TGV) (Bredies et al., 2010) for optimisation. Guided techniques use another image aligned with the depth-map to inform the refinement. The guide image is used especially around edges, to modulate the smoothing effect of filtering or optimisation. For example, Kopf et al. (2007) or Matsuo et al. (2013) propose variants of a JBF for refining depth, while Tanner et al. (2016) demonstrates a TGV-based method that uses both magnitude and direction of colour images to regularise depth maps. An interesting combination of learning and optimisation is proposed by Riegler et al. (2016). The Primal-Dual algorithm (Chambolle and Pock, 2011) normally employed for TGV optimisation is unrolled and included into a CNN model that learns to upsample depth images. Our work relies on an existing 3D reconstruction pipeline (Tanner et al., 2015), in which some of these depth refinement techniques have already been employed. We focus on post-processing meshes and fixing errors that cannot easily be fixed in single, live depth images.

Learnt Depth Refinement and Completion

Some methods for *learning* depth map refinement and completion have been recently proposed. Eldesokey et al. (2018); Uhrig et al. (2017) propose CNN model for solving the KITTI Depth Completion Challenge, where sparse depth maps produced from laser data are densified. Hua and Gong (2018) use normalised convolutions (Knutsson and Westin, 1993) to predict dense depth maps that have been sparsely sampled. These methods all rely on having some sort of high-quality, usually laser, depth information (albeit sparse) at run-time, and are only designed to fill in the missing data. In contrast, we only require high-quality data during training, and our method aims to refine depth from a low-quality mesh in a more general sense – both filling in blanks, as well as refining existing surfaces.

A few other methods more closely related in spirit to ours aim to learn depth refinement using meshes as reference. Kwon et al. (2015) use dictionary learning

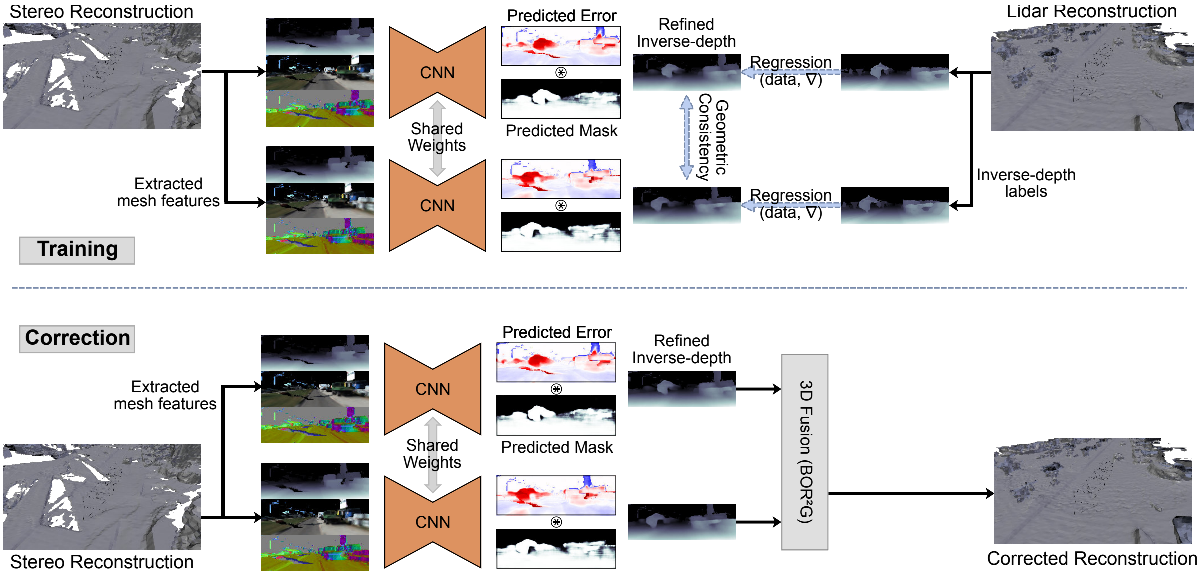

Figure 2: Overview of our method. Our network learns to correct meshes by observing 2D renderings of mesh features and predicting the error in inverse-depth. In addition to error, our network also predicts a soft mask that is multiplied element-wise with the error to control which regions of the input inverse-depth image are corrected. During training, inverse-depth images from a high-quality reconstruction are used to supervise our network, and a geometric consistency loss is applied between predictions on nearby views, as described in Section 3.2. When using our model to correct meshes, the refined inverse-depth images of the input mesh are fused into a new 3D reconstruction of higher quality.

to model the statistical relationships between raw RGB-D images, and high-quality depth data obtained by fusing multiple depth maps with KinectFusion (Newcombe et al., 2011). Two other recent works use fused RGB-D reconstruction to obtain high-quality reference data and train CNNs to enhance depth. Zhang and Funkhouser (2018) uses a colour image to predict normals and occlusion boundaries, supervised by the 3D reconstruction, and then formulates an optimisation problem to fill in holes in an aligned depth image. Jeon and Lee (2018) introduce a 4000-image dataset of raw/clean depth image pairs, and train a CNN to enhance raw depth maps. Furthermore, they show that 3D reconstructions can be obtained with fewer data and quicker when using their depth-enhancing network. These methods all rely on live colour images to guide the refinement or completion of live depth. That means that only limited data is available for training. In contrast, our purely mesh-based formulation allows us to extract many more training pairs from any viewpoint, removing any viewpoint-specific bias that might otherwise surface while learning.

Learnt Depth Estimation

Another related line of research has been monocular depth estimation, which inspires our choices of network architecture and the use of geometry as a source of self-supervision. Dharmasiri et al. (2019); Godard et al. (2017); Klodt and Vedaldi (2018); Laina et al. (2016); Mahjourian et al. (2018); Ummenhofer et al. (2017); Zhou et al. (2017), etc. propose various CNN models for depth estimation from single colour images. When explicit depth ground-truth is unavailable, the training is self-supervised using multiview geometry: the predicted depths and relative poses should maximise the photometric consistency of nearby input images. In this work, we show how the photometric consistency loss can be adapted to ensure consistency between inverse-depth predictions directly, without need for colour images.

3 METHOD

3.1 Training Data

In contrast to many existing approaches, this work is about correcting *existing* reconstructions, and therefore we assume the existence of 3D meshes of a scene. In addition to the low-quality reconstruction we wish to correct, we also have a high-quality reconstruction of the same scene. For example, we learn to correct 3D reconstructions from depth-maps using laser reconstructions as a reference. To build the meshes we train on, we use the BOR^{2}G (Tanner et al., 2015) system.

The training data consists of 2D views of the

(a) Colour Reconstruction

(b) Inverse-depth

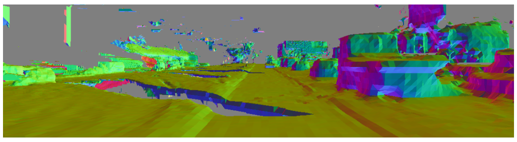

(c) Triangle Surface Normal

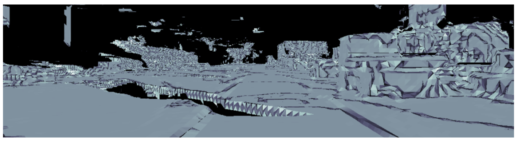

(d) Triangle Area

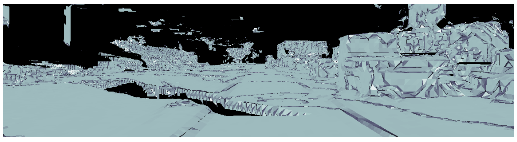

(e) Triangle Edge Length Ratios

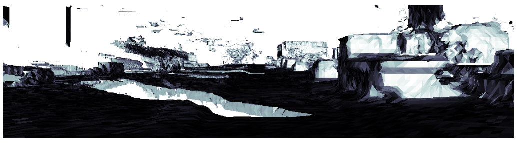

(f) Surface to Camera Angle

Figure 3: Example mesh features. We fly a camera through an existing mesh and at each location produce mesh features. During training, inverse-depth images of a high-quality mesh are available, and our model learns a mapping from the mesh features pictured above to the high-quality inverse-depth.

meshes. We use the same virtual camera to generate aligned views of the low-quality mesh and the high-quality mesh for each scene. Because a mesh is available, we can generate multiple types of images at each viewpoint. In particular, we generate inverse-depth, normals, mesh triangle area, mesh triangle edge ratio (ratio between the shortest and the longest edge of each triangle), and surface-to-camera angle (Figure 3). We refer to these images as *mesh features*. The ground-truth labels (Δ) are computed as the difference in inverse-depth between high-quality and low-quality reconstructions:

$$\Delta(p) = d^{hq}(p) - d^{lq}(p) \tag{1}$$

where p is a pixel index, and d^{hq} and d^{lq} are inverse-depth images for the high-quality and low-quality reconstruction, respectively. For notational compactness, $\Delta(p)$ is referred to as Δ, and future definitions are over all values of p, unless otherwise mentioned.

Inverse-depth is used instead of depth for several reasons. Firstly, it emphasises surfaces close to the camera where more information is available per pixel. Secondly, background (non-surface) pixels are not processed separately – they are assigned a value of zero, corresponding to points infinitely far away from the camera. If we used depth, those pixels would either have to be assigned an arbitrary finite value, which would result in semantic discontinuities in the output, or learnt to be ignored by the network, since there is no standard way to deal with infinite values in a CNN. Finally, another advantage of inverse-depth is that resampling it, which is needed to compute geometric consistency, is simpler than resampling depth images.

3.2 Geometric Consistency

Intuitively, since the reconstructions we wish to correct are static, the predictions made from overlapping views should be geometrically consistent. In other words, surfaces that appear in a certain location according to a prediction should appear in the same location in all predictions where they are in view.

We resample nearby predicted views according to the predicted geometry of the current view, and minimise the absolute difference in inverse-depth. This dense warping is similar to reprojecting nearby views into the current view, but has the advantage of being differentiable, and of generating dense images instead of sparse reprojected pointclouds. An illustration of this idea is shown in Figure 1.

Normally, dense warping is used in conjunction with colour images, where the values of the pixels are view-independent. Since we are warping inverse-depth images, where the pixel values depend on the viewpoint, we need to compute the absolute difference in the same camera frame.

Concretely, for a view t, a nearby view n, let Δ_t^* be a CNN prediction for the target view, let Δ_n^* be a prediction for the nearby view, and let $d_t^* = d_t^{lq} + \Delta_t^*$ and $d_n^* = d_n^{lq} + \Delta_n^*$ the corrected inverse-depth images for the two views. Furthermore, let $\mathbf{p}_t$ be pixel coordinates in the target view, K the intrinsic matrix of the virtual camera, and $T_{n,t}$ the SE(3) transform from view t to view n. We can then define the geometric

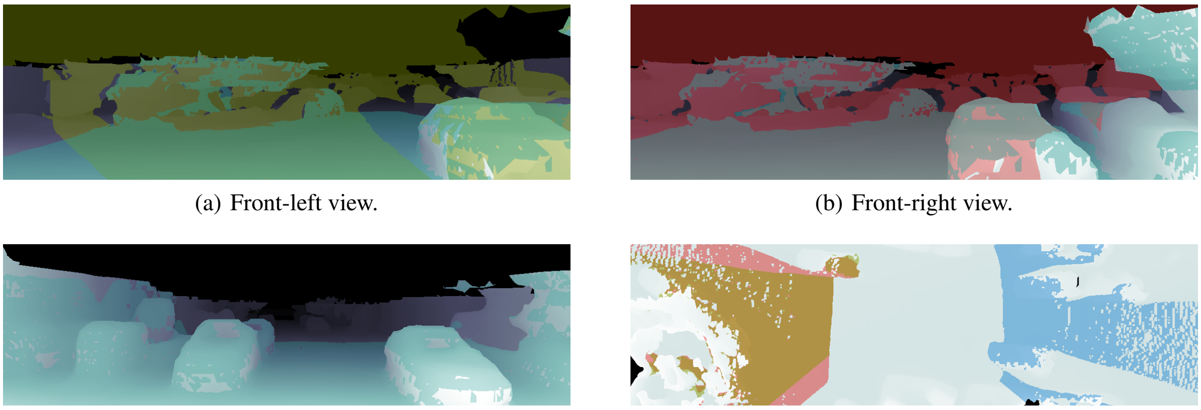

(a) Front-left view.
(b) Front-right view.
(c) Back view.
(d) Top view.

Figure 4: Visibility masks for views generated at a location. The image regions highlighted in red, green, blue, and cyan are also visible in the (a) left, (b) right, (c) back, and (d) top views, respectively. (a): inverse-depth view from a dense 3D reconstruction; the regions visible in the left, and top views are respectively highlighted in green and cyan. (b): a view of the same scene as (a), 2 m to the right; the regions visible in the left, and top views are respectively highlighted in red and cyan. (c): a view of the same scene as (a), looking back; the region visible in top view is highlighted in cyan. (d): a view of the same scene as (a), looking down from 25 m above; the regions visible in the left, right, and back views are respectively highlighted in red, green, and blue. Areas outside the highlighted regions are occluded – they are not visible from the other view. For example, distant areas of (a)–(c), such as the sky, are not visible from the top view; the region behind the car on the right in (a) is not visible from (b). These occluded parts of the image are ignored when computing the geometric consistency loss (Section 3.3.2). For visualisation purposes, morphological closing has been applied to the visibility masks shown here, to remove some of the small-scale noise.

inconsistency $d^*_{n,t} - \widetilde{d}^*_{n,t}$ where $d^*_{n,t}$ is the predicted inverse-depth from view t in the frame of view n and $\widetilde{d}^*_{n,t}$ is the warped inverse-depth from view n.

They are defined as follows:

$$\widetilde{d}^*_{n,t}(\mathbf{p}_t) = d^*_n(\mathbf{p}_n), \tag{2}$$

$$d^*_{n,t}(\mathbf{p}_t) = \frac{\mathbf{x}_n^{(4)}}{\mathbf{x}_n^{(3)} + \varepsilon}, \tag{3}$$

where superscripts indicate vector elements, $\mathbf{x}_n$ is the 3D homogeneous point in view n corresponding to pixel $\mathbf{p}_t$, and $\mathbf{p}_n$ its projection:

$$\mathbf{p}_n = \frac{1}{\mathbf{x}_n^{(3)} + \varepsilon}\left(\mathbf{x}_n^{(1)}\ \mathbf{x}_n^{(2)}\right)^T, \tag{4}$$

$$\mathbf{x}_n = F_h \mathbf{x}_t, \tag{5}$$

$$\mathbf{x}_t = \left(\mathbf{p}_t\ 1\ d^*_t(\mathbf{p}_t)\right)^T, \tag{6}$$

$$F_h = K_h T_{n,t} K_h^{-1}, \tag{7}$$

$$K_h = \begin{pmatrix} K & \mathbf{0} \\ \mathbf{0}^T & 1 \end{pmatrix}. \tag{8}$$

The sample pixel $\mathbf{p}_n$ does not necessarily have integer coordinates, and thus may lie in-between pixels in the d^*_n grid. Note that we add a small value ε with the same sign as $\mathbf{x}_n^{(3)}$ in Equations 3 and 4 to avoid dividing by zero. Under the mild assumption that surfaces between pixels are planar, we can sample d^*_n by linearly interpolating the four pixels nearest to $\mathbf{p}_n$ – another advantage of the inverse-depth formulation.

Occlusion Masks

A common problem with this approach is that views cannot be consistent in the presence of occlusions. In our setting, however, since the views are synthetic (and therefore the intrinsic and extrinsic parameters are perfectly known), we are able to create occlusion masks and only apply the geometric consistency loss where there are no occlusions, as noted in Equation 11.

We compute occlusion masks from the reference high-quality reconstruction. Each mesh triangle is assigned an index by hashing its world frame coordinates. Then, in addition to mesh features, an image with mesh triangle indices is generated at each location. For each pair of views, each pixel of the triangle index image is resampled from one view into the other in a similar fashion to the inverse-depth above. Instead of interpolating between the four nearest neighbours, these are returned as four separate samples. The pixels where the indices match at least one of the four samples are considered unoccluded, and the pixels where they do not are considered occluded (see Figure 4).

Small errors appear due to rasterisation when mesh triangles are too small, often those that are far away from the camera. We could avoid these errors by generating occlusion masks with the OpenGL rasterisation

Table 1: Overview of the CNN architecture for error prediction.

Block Type	Filter Size/Stride	Output Size
Input	-	$96 \times 288 \times F$
Convolution	$3 \times 3/1$	$96 \times 288 \times 64$
Residual	$3 \times 3/1$	$96 \times 288 \times 64$
Convolution	$5 \times 5/1$	$48 \times 144 \times 64$
Max Pool	$3 \times 3/2$	$24 \times 72 \times 64$
Residual$\times 2$	$3 \times 3/1$	$24 \times 72 \times 64$
Projection	$3 \times 3/2$	$12 \times 36 \times 256$
Residual$\times 2$	$3 \times 3/1$	$12 \times 36 \times 256$
Projection	$3 \times 3/2$	$6 \times 18 \times 512$
Residual$\times 2$	$3 \times 3/1$	$6 \times 18 \times 512$
Projection	$3 \times 3/2$	$3 \times 9 \times 1024$
Residual$\times 8$	$3 \times 3/2$	$3 \times 9 \times 2048$
Up-projection	$3 \times 3/\frac{1}{2}$	$6 \times 18 \times 1024$
Up-projection	$3 \times 3/\frac{1}{2}$	$12 \times 36 \times 512$
Up-projection	$3 \times 3/\frac{1}{2}$	$24 \times 72 \times 256$
Up-projection	$3 \times 3/\frac{1}{2}$	$48 \times 144 \times 128$
Up-projection	$3 \times 3/\frac{1}{2}$	$96 \times 288 \times 32$
Residual	$3 \times 3/1$	$96 \times 288 \times 32$
Convolution	$3 \times 3/1$	$96 \times 288 \times 2$

pipeline when the rest of the data is generated. However, this greatly increases the space required to store training data – the number of occlusion masks scales quadratically with the number of views we want to enforce consistency between. Generating the occlusion masks on the fly means that geometric consistency can be enforced between arbitrary views, so more settings can be explored without regenerating part of the training data.

3.3 Model

3.3.1 Network Architecture

The model used is an encoder-decoder CNN similar to the one proposed in Tanner et al. (2018). The encoder is composed of residual blocks based on the ResNet-50 architecture (He et al., 2016), and the decoder uses up-convolutions proposed by Shi et al. (2016). U-Net Ronneberger et al. (2015) style skip connections are added between the encoder and the decoder to improve the sharpness of predictions. As a simple way to offer our model some introspective capabilities, we predict a soft attention mask (with values $\in [0,1]$) in addition to the error in inverse-depth, as a second output of the network. This mask is multiplied pixel-wise with the error prediction to modulate which parts are going to be used and does not require extra supervision. Table 1 provides an overview for each of the layers of the proposed CNN.

3.3.2 Loss

The objective function has several components, as follows. The first term is the data loss that minimises the error between the output and the label. To compute this loss, we use berHu norm (Owen, 2007). For large errors, this behaves in the same way as an L_2 norm. For small errors, where the gradients of L_2 become too small to drive the error completely to zero, L_1 norm is used instead. The advantages of this norm have also been observed in Laina et al. (2016); Ma and Karaman (2018). The data loss is defined as follows:

$$\mathcal{L}^{data} = \sum_{p \in V} \mathrm{W} \cdot \|\Delta^* - \Delta\|_{berHu}, \tag{9}$$

where p is the pixel index, V is the set of valid pixels (to account for missing data in the ground-truth), W is a per-pixel weight detailed in Section 3.3.3, Δ^* and Δ are the prediction and the target, respectively, and $\|\cdot\|_{berHu}$ is the berHu norm.

To improve small-scale details and prevent artefacts in the prediction, while also allowing for sharp discontinuities, we also apply a loss on the gradient of the predictions:

$$\mathcal{L}^{\nabla} = \frac{1}{2} \sum_{p \in V} \mathrm{W} \cdot \left(|\partial_x \Delta^* - \partial_x \Delta| + \left|\partial_y \Delta^* - \partial_y \Delta\right| \right). \tag{10}$$

We use the Sobel operator (Sobel and Feldman, 1968) to approximate the gradients in the equation above.

The geometric consistency loss guides nearby predictions to have the same 3D geometry, and relies on reprojected nearby views $\widetilde{d}^*_{n,t}$. For a target view t, a set of nearby views N, the set of pixels unoccluded in a nearby view U_n (see Figure 4), this loss is defined as:

$$\mathcal{L}^{gc} = \sum_{n \in N} \sum_{p \in U_n} \left| \widetilde{d}^*_{n,t} - d^*_{n,t} \right|. \tag{11}$$

Note that U_n has no relation to the set of valid pixels (V) from the previous losses, since this loss is only computed between predictions. This enables the network to make sensible predictions even in parts of the image which have no valid label.

Finally, we also include an L_2 weight regulariser, $\mathcal{L}^{reg}$, to reduce overfitting by keeping the weights small. The overall objective is thus defined as:

$$\mathcal{L} = \lambda^{data} \mathcal{L}^{data}_s + \lambda^{\nabla} \mathcal{L}^{\nabla} + \lambda^{gc} \mathcal{L}^{gc} + \lambda^{reg} \mathcal{L}^{reg}, \tag{12}$$

where s is the scale, and the λs are weights for each of the components (see Table 2 for values).

3.3.3 Loss Weight

Inspired by the work of Ronneberger et al. (2015) on U-Nets, we use a loss-weighting mechanism based on

Table 2: Summary of Hyperparameters Used in System.

Symbol	Value	Description
λ^{data}	1	Weight of the data loss.
λ^{∇}	0.1	Weight of the smoothness loss.
λ^{gc}	0.1	Weight of the geometric consistency loss.
λ^{reg}	10^{-6}	Weight of the L_2 variable regulariser.
w_{min}	0.1	Minimum per-pixel loss scaling.
w_{max}	5	Maximum per-pixel loss scaling.
η_{max}	10^{-4}	Initial learning rate.
η_{min}	$5 \cdot 10^{-6}$	Final learning rate.
T_{max}	$1.2 \cdot 10^{5}$	Learning rate decay steps.
β_1	0.9	Adam exponential decay rate for first moment estimates.
β_2	0.999	Adam exponential decay rate for second moment estimates.
	80	Norm at witch gradients are clipped during training.
	16	Batch size.
	$5 \cdot 10^{5}$	Number of training steps.

the Euclidean Distance Transform (Felzenszwalb and Huttenlocher, 2012) to emphasise edge pixels when regressing to the error in depth. We first extract Canny edges (Canny, 1986) from the ground-truth labels. Based on these edges, we then compute the per-pixel weights as:

$$\begin{aligned} d(p) &= \ln(1 + \mathrm{EDT}(p)) \\ \mathrm{W}(p) &= (w_{max} - w_{min}) \left(1 - \frac{d(p)}{\max_p d(p)}\right) + w_{min} \end{aligned}, \tag{13}$$

where $\mathrm{W}(p)$ is the loss weight for pixel p, $\mathrm{EDT}(p)$ is the Euclidean Distance Transform at pixel p, and w_{min} and w_{max} are the desired range of the per-pixel weight. This will assign w_{max} weight to edge pixels, and lower weights the farther pixels are from an edge, down to w_{min} for the farthest pixels.

4 EXPERIMENTS

4.1 Experimantal Setup

Training and Inference

The network is implemented in Python using TensorFlow v1.12. Each model is trained on an Nvidia Titan V GPU. The weights are optimised for 500 000 steps with a batch size of 16 using the Adam optimiser (Kingma and Ba, 2015). The learning rate (η_t) is decayed linearly for the first 120 000 steps. Generating the mesh features takes an average of 52 ms per view using OpenGL on an Nvidia GTX Titan Black,

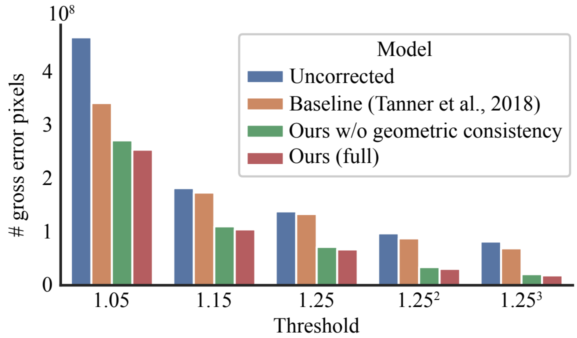

Figure 5: Gross error correction. For each threshold (Equation 14), we count how many pixels are incorrect in the predictions over the test set. Our full model removes 45.3% of the smaller errors and 77.5% of the gross errors. The baseline model is unable to effectively handle the multi-view setup, and fails to correct gross errors.

and inference takes an average of 12.5 ms on the Titan V. All the training hyper-parameters are defined in Table 2. The optimiser parameters are the ones sugested by Kingma and Ba (2015), while the rest have been chosen after a small search to improve validation metrics.

Dataset

Three sequences from the KITTI visual odometry (KITTI-VO) dataset were used as the input to the reconstruction pipeline. For each sequence, two reconstructions are built: one from the stereo camera depth-maps, and one from the laser data. Both the meshes are generated with a fixed voxel width of 0.2 m. In the experiments, we show how to learn a correction of the depth-map reconstruction using the laser reconstruction as reference. Using OpenGL Shading Language (GLSL), we create a virtual camera and project each dense reconstruction into mesh features. We sample locations along the original trajectory in each sequence every 0.3m, and at each location we generate mesh features from four different viewpoints. An illustration of the viewpoints is shown in Figure 4. For all experiments, the KITTI-VO sequences 00, 05, and 06 are used, from which a total of 96 728 training examples of size 96×288 are generated. We split each of the mesh feature sequences into three distinct parts: the first 80% we use as training data, the next 10% we use for validating hyperparameter choices, and the last 10% we use for evaluation. All three sequences are predominantly in urban environments with small amounts of visible vegetation.

Performance Metrics

We use some metrics common in literature for assessing inverse-depth predictions.

Table 3: Generalisation Capability of Depth Error Correction.

Model	Train	Test	iMAE	iRMSE	$\delta < 1.05$	$\delta < 1.15$	$\delta < 1.25^1$	$\delta < 1.25^2$	$\delta < 1.25^3$
Uncorrected	–	00	$1.76 \cdot 10^{-2}$	$8.10 \cdot 10^{-2}$	52.71%	79.00%	84.02%	88.73%	90.71%
——‖——	–	05	$1.57 \cdot 10^{-2}$	$8.15 \cdot 10^{-2}$	55.11%	80.61%	84.27%	88.30%	90.46%
——‖——	–	06	$2.81 \cdot 10^{-2}$	$1.24 \cdot 10^{-1}$	49.47%	72.71%	75.07%	78.64%	80.49%
Ours	05; 06	00	$1.45 \cdot 10^{-2}$	$8.03 \cdot 10^{-2}$	66.14%	85.27%	89.93%	94.76%	96.82%
——‖——	00; 06	05	$1.19 \cdot 10^{-2}$	$7.67 \cdot 10^{-2}$	70.38%	86.31%	90.25%	94.86%	96.99%
——‖——	00; 05	06	$2.37 \cdot 10^{-2}$	$1.15 \cdot 10^{-1}$	62.27%	78.14%	81.72%	85.85%	88.20%

Table 4: Depth Error Correction Ablation Study Results.

Model	iMAE	iRMSE	$\delta < 1.05$	$\delta < 1.15$	$\delta < 1.25$	$\delta < 1.25^2$	$\delta < 1.25^3$
Uncorrected	$1.85 \cdot 10^{-2}$	$8.73 \cdot 10^{-2}$	50.90%	80.77%	85.38%	89.72%	91.35%
Baseline	$1.47 \cdot 10^{-2}$	$6.25 \cdot 10^{-2}$	63.92%	81.65%	85.90%	90.72%	92.69%
w/ our losses; no GC	$1.28 \cdot 10^{-2}$	$6.26 \cdot 10^{-2}$	67.77%	84.35%	89.05%	94.16%	96.17%
w/ our losses; GC	$1.17 \cdot 10^{-2}$	$5.44 \cdot 10^{-2}$	68.66%	84.64%	89.45%	94.81%	96.65%
Ours (no attn; no GC)	$1.12 \cdot 10^{-2}$	$5.49 \cdot 10^{-2}$	70.47%	87.68%	92.08%	96.35%	97.72%
Ours (no GC)	$1.12 \cdot 10^{-2}$	$5.63 \cdot 10^{-2}$	71.31%	88.34%	92.41%	96.41%	97.81%
Ours (no attn)	$\mathbf{1.02 \cdot 10^{-2}}$	$\mathbf{5.31 \cdot 10^{-2}}$	*72.93%*	**89.27%**	**93.20%**	**96.87%**	**98.10%**
Ours (full)	*$1.06 \cdot 10^{-2}$*	*$5.37 \cdot 10^{-2}$*	**73.16%**	*88.94%*	*92.91%*	*96.76%*	*98.05%*

Our first metric measures the accuracy of our network's ability to estimate errors under a given threshold, serving as an indication of how often our estimate is correct. The thresholded accuracy measure is essentially the expectation that a given pixel in V is within a threshold thr of the label:

$$\delta = \mathbb{E}_{p \in V} \left[\mathbb{I} \left(\max \left(\frac{d^{hq}}{d^*}, \frac{d^*}{d^{hq}} \right) < thr \right) \right], \qquad (14)$$

where d^{hq} is the reference inverse-depth, d^* is the predicted inverse depth, V is the set of valid pixels, and n is the cardinality of V, and $\mathbb{I}(\cdot)$ represents the indicator function. For granularity, we use $thr \in \{1.05, 1.15, 1.25, 1.25^2, 1.25^3\}$.

In addition, the mean absolute error (MAE) and root mean square error (RMSE) metrics provide a quantitative measure of per pixel error and are computed as follows:

$$\text{iMAE} = \frac{1}{n} \sum_{p \in V} \left| d^* - d^{hq} \right|, \qquad (15)$$

$$\text{iRMSE} = \sqrt{\frac{1}{n} \sum_{p \in V} (d^* - d^{hq})^2}, \qquad (16)$$

where the 'i' indicates that the metrics are computed over inverse-depth images.

4.2 Gross Error Correction

We first look at how well our model corrects gross errors in inverse-depth. Equation 14 can be used to classify pixels in an image as either correct or incorrect at a given threshold. Using this method, we count the number of incorrect pixels in our predictions, and compare it to the number of incorrect pixels in the input inverse-depth. As a baseline, we train the model proposed in Tanner et al. (2018) on our dataset, and compare it to our full model, trained with and without the geometric consistency loss (Figure 5). Our proposed model outperforms the baseline at correcting both small errors ($thr = 1.05$) as well as larger errors, reducing the number of errors at $thr = 1.25^3$ by 77.5%.

4.3 Generalisation Capability

To be useful in practice, the model needs to be able to generalise to new data. For example, separate models could be trained for indoor scenes and outdoor scenes, or other different types of environments, but certainly within the same kind of environment, one model should work well for a variety of scenes.

To evaluate this, we train the full model on a subset of the available sequences, and test it on the rest (excluding the frames used for validation in Section 4.2). Sequences 00 and 05 represent different suburban scenes of the same city, while the scene in sequence 06 is in an area where the road is much wider and the buildings are much farther apart. Table 3 shows the data splits and the performance of the models on the test sequences. Interestingly, the model trained only on the suburban scenes of sequences 00 and 05 performs particularly well on the visually distinct sequence 06.

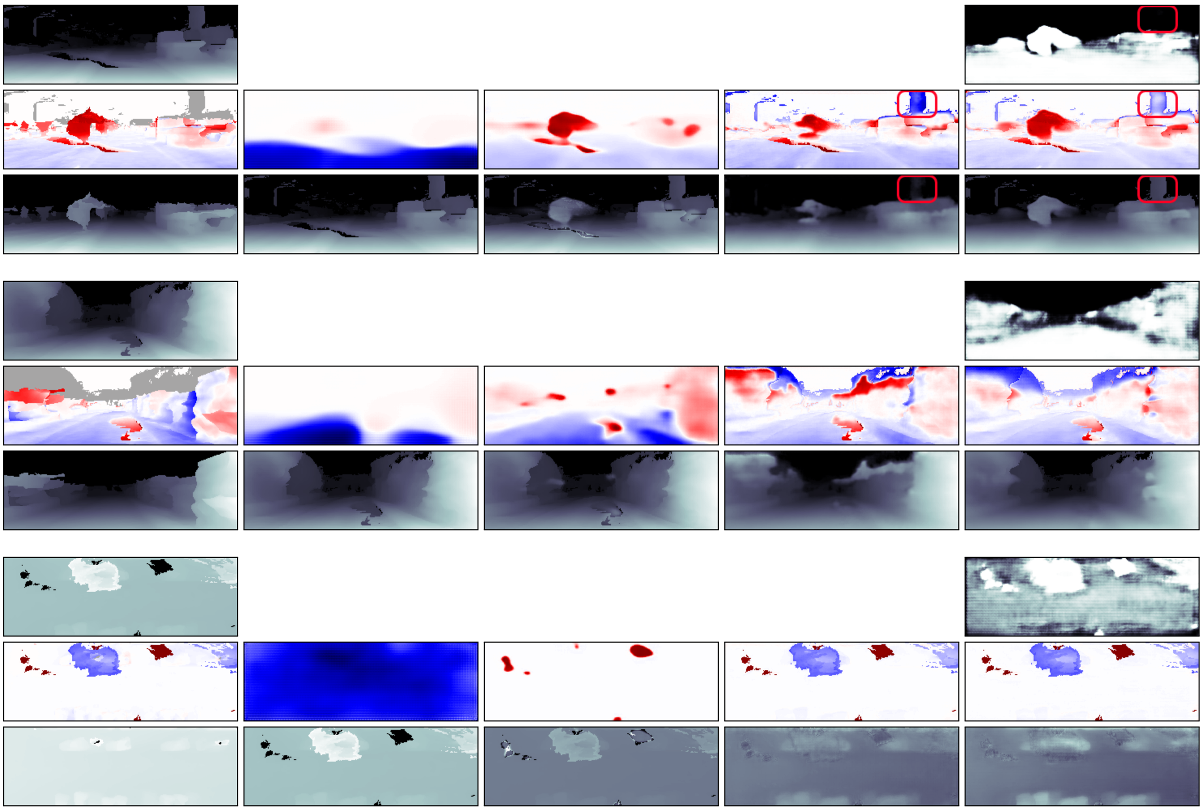

(a) Ground truth (b) Baseline (c) Baseline + our losses (d) Ours (no attn; no GC) (e) Ours (full)

Figure 6: Illustration of how the quality of the predictions changes as different components are added to the system. Each three rows show an example, as follows: (a) Input inverse-depth and ground-truth error, and ground-truth inverse-depth. The shaded areas in the ground-truth error represent missing data in the reference mesh. (b)–(d) Prediction and corrected inverse-depth. (e): Attention mask, prediction, and corrected inverse-depth. The baseline model (b) only learns very rough predictions and is unable to generalise well to the top viewpoint (last example). Our proposed losses help with generalisation across viewpoints, but without skip connections in the network predictions are not very well localised (c). Our model (d); (e) makes well-localised predictions. The attention mask removes some of the spurious predictions where there is no reference data (e). For example, the highlighted background structure in the first example is removed when the attention mask is not used (d), while the attention mask disables edits to that region of the input image (e).

This highlights the ability of our model to reduce gross errors.

4.4 Ablation Study

To better understand how different components of our model improve the learnt correction, we perform an ablation study. The results in Table 4 show that our proposed geometric consistency loss (rows with GC) improves performance at all error scales.

The proposed attention mask (rows with attn) improves the performance in the absence of geometric consistency, but slightly limits the performance especially with larger errors. However, qualitatively (Figure 6), the attention mask allows us to better handle missing training data (that is greyed out in the ground truth column). In particular, surfaces are not spuriously removed or added in those regions: the model learns to mask those regions out of the correction and keep them as they are.

4.5 Corrected Meshes

We demonstrate our method in practice by using the corrected inverse-depth images to create new, corrected reconstructions of the input meshes. Our model effectively corrects missing surfaces, particularly on the road, as illustrated in Figure 7. This results in higher surface coverage of the original scene.

As is common with neural networks trained for image regression, predictions can sometimes be too smooth. While we address this by using skip connec-

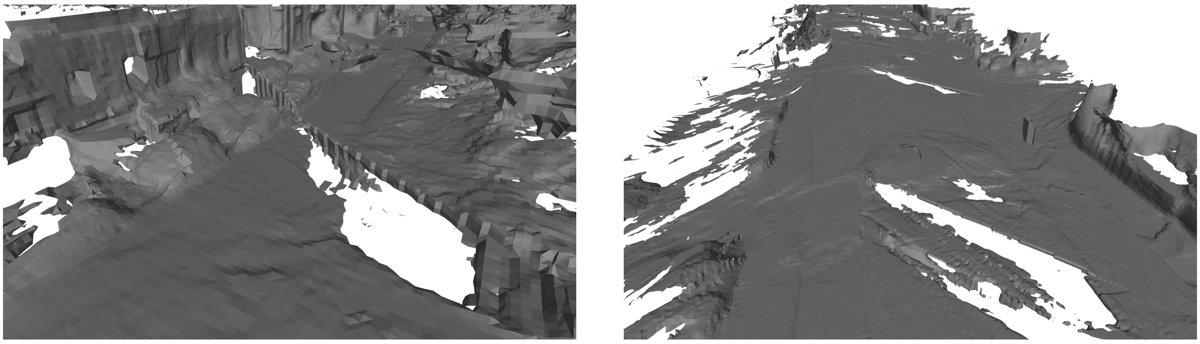

(a) Uncorrected mesh

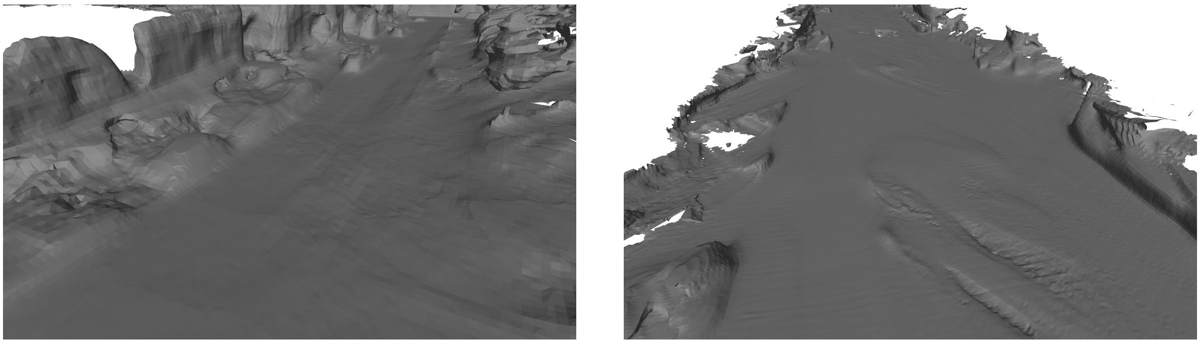

(b) Corrected mesh

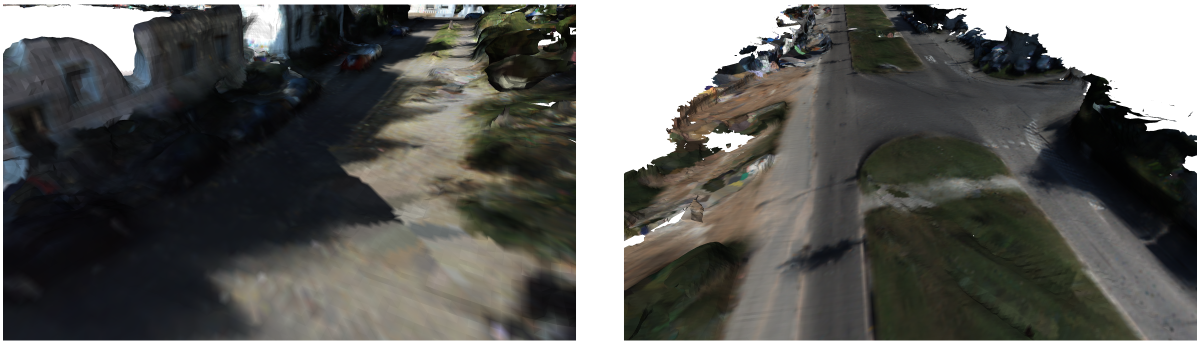

(c) Full colour reconstruction

Figure 7: Images of 3D reconstructions of KITTI sequence 00 (left) and 06 (right). (a) Shows the uncorrected meshes that our network processes, built solely from a stereo camera. Note the large missing surfaces due to either poor lighting, or poorly textured regions. Our model recovers the missing surfaces (b), providing a more complete reconstruction. (c) shows the corrected meshes with colour copied from the uncorrected input. The models used for this illustration here are trained as described in Section 4.3, so the corrected meshes are not part of the training data.

tions between the encoder and decoder of the network, smoothness in predictions can still occur, especially when there are no edges in the network input to guide the output. This is not a problem when filling in closed holes like the ones in the road, which have clear boundaries. However, for regions without clear boundaries, such as the top of buildings, network predictions are too smooth. This can be seen in both Figure 6 and Figure 7.

5 CONCLUSION

In this paper we present a method for correcting gross errors in dense 3D meshes. We extracted paired 2D mesh features from two reconstructions and trained a neural network to predict the difference in inverse-depth between the two. We addressed the issue of overly-smooth predictions with a U-Net architecture and a loss-weighting mechanism that emphasises edges. The geometric consistency of our predictions is improved with a view-synthesis loss that targets inconsistencies. Our experiments show that the proposed method reduces gross errors in inverse-depth views of the mesh by up to 77.5%.

While in this paper we focus on correcting meshes of urban scenes built from street-level sensors, our method is generally applicable to environments with strong priors that can be learnt from data.

ACKNOWLEDGEMENTS

The authors would like to acknowledge the support of the UK's Engineering and Physical Sciences Research Council (EPSRC) through the Centre for Doctoral Training in Autonomous Intelligent Machines and Systems (AIMS) Programme Grant EP/L015897/1. Paul Newman is supported by EPSRC Programme Grant EP/M019918/1.

REFERENCES

Bredies, K., Kunisch, K., and Pock, T. (2010). Total generalized variation. *SIAM Journal of Imaging Sciences*, 3:4920–526.

Canny, J. F. (1986). A computational approach to edge detection. *IEEE Transactions on Pattern Analysis and Machine Intelligence*, PAMI-8:679–698.

Chambolle, A. and Pock, T. (2011). A first-order primal-dual algorithm for convex problems with applications to imaging. *Journal of Mathematical Imaging and Vision*, 40(1):120–145.

Dharmasiri, T., Spek, A., and Drummond, T. (2019). ENG: End-to-end neural geometry for robust depth and pose estimation using CNNs. In *Proceedings of the Asian Conference on Computer Vision (*ACCV*)*, pages 625–642.

Eldesokey, A., Felsberg, M., and Khan, F. S. (2018). Propagating confidences through CNNs for sparse data regression. In *Proceedings of the British Machine Vision Conference (*BMVC*)*.

Felzenszwalb, P. F. and Huttenlocher, D. P. (2012). Distance transforms of sampled functions. *Theory of Computing*, 8:415–428.

Godard, C., Mac Aodha, O., and Brostow, G. J. (2017). Unsupervised monocular depth estimation with left-right consistency. In *Proceedings of the IEEE International Conference on Computer Vision and Pattern Recognition (*CVPR*)*.

He, K., Zhang, X., Ren, S., and Sun, J. (2016). Deep residual learning for image recognition. In *Proceedings of the IEEE International Conference on Computer Vision and Pattern Recognition (*CVPR*)*, pages 770–778.

Hua, J. and Gong, X. (2018). A normalized convolutional neural network for guided sparse depth upsampling. In *Proceedings of the International Joint Conference on Artificial Intelligence (*IJCAI*)*.

Jeon, J. and Lee, S. (2018). Reconstruction-based pairwise depth dataset for depth image enhancement using CNN. In *Proceedings of the European Conference on Computer Vision (*ECCV*)*.

Kingma, D. and Ba, J. (2015). Adam: A method for stochastic optimization. In *Proceedings of the International Conference on Learning Representations (*ICLR*)*.

Klodt, M. and Vedaldi, A. (2018). Supervising the new with the old: Learning SfM from SfM. In *Proceedings of the European Conference on Computer Vision (*ECCV*)*.

Knutsson, H. and Westin, C.-F. (1993). Normalized and differential convolution: Methods for interpolation and filtering of incomplete and uncertain data. In *Proceedings of the IEEE International Conference on Computer Vision and Pattern Recognition (*CVPR*)*.

Kopf, J., Cohen, M. F., Lischinski, D., and Uyttendaele, M. (2007). Joint bilateral upsampling. *ACM Transactions on Graphics*, 26:96.

Kwon, H., Tai, Y.-W., and Lin, S. (2015). Data-driven depth map refinement via multi-scale sparse representation. In *Proceedings of the IEEE International Conference on Computer Vision and Pattern Recognition (*CVPR*)*, pages 159–167.

Laina, I., Rupprecht, C., Belagiannis, V., Tombari, F., and Navab, N. (2016). Deeper depth prediction with fully convolutional residual networks. In *Proceedings of the IEEE International Conference on 3D Vision (*3DV*)*, pages 239–248.

Ma, F. and Karaman, S. (2018). Sparse-to-dense: Depth prediction from sparse depth samples and a single image. In *Proceedings of the IEEE International Conference on Robotics and Automation (*ICRA*)*.

Mahjourian, R., Wicke, M., and Angelova, A. (2018). Unsupervised learning of depth and ego-motion from monocular video using 3D geometric constraints. In *Proceedings of the IEEE International Conference on Computer Vision and Pattern Recognition (*CVPR*)*, pages 5667–5675.

Matsuo, T., Fukushima, N., and Ishibashi, Y. (2013). Weighted joint bilateral filter with slope depth compensation filter for depth map refinement. In *Proceedings of the International Conference on Computer Vision Theory and Applications (*VISAPP*)*.

Newcombe, R. A., Izadi, S., Hilliges, O., Molyneaux, D., Kim, D., Davison, A. J., Kohli, P., Shotton, J., Hodges, S., and Fitzgibbon, A. W. (2011). KinectFusion: Real-time dense surface mapping and tracking. In *IEEE International Symposium on Mixed and Augmented Reality*, pages 127–136.

Owen, A. B. (2007). A robust hybrid of lasso and ridge regression. *Contemporary Mathematics*, 443:59–72.

Riegler, G., Rüther, M., and Bischof, H. (2016). ATGV-Net: Accurate depth super-resolution. In *Proceedings of the European Conference on Computer Vision (*ECCV*)*.

Ronneberger, O., Fischer, P., and Brox, T. (2015). U-Net: Convolutional networks for biomedical image segmentation. In *Medical Image Computing and Computer Assisted Intervention (*MICCAI*)*.

Shi, W., Caballero, J., Huszár, F., Totz, J., Aitken, A. P., Bishop, R., Rueckert, D., and Wang, Z. (2016). Real-time single image and video super-resolution using an efficient sub-pixel convolutional neural network. In *Proceedings of the IEEE International Conference on Computer Vision and Pattern Recognition (*CVPR*)*, pages 1874–1883.

Sobel, I. and Feldman, G. (1968). A 3×3 isotropic gradient operator for image processing. presented at the Stanford Artificial Intelligence Project (SAIL).

Tanner, M., Piniés, P., Paz, L. M., and Newman, P. (2015). BOR^{2}G: Building optimal regularised reconstructions with GPUs (in cubes). In *Proceedings of the International Conference on Field and Service Robotics (*FSR*)*, Toronto, Canada.

Tanner, M., Piniés, P., Paz, L. M., and Newman, P. (2016). Keep geometry in context: Using contextual priors for very-large-scale 3d dense reconstructions. In *Robotics: Science and Systems (*RSS*). Workshop on Geometry and Beyond: Representations, Physics, and Scene Understanding for Robotics*.

Tanner, M., Săftescu, Ș., Bewley, A., and Newman, P. (2018). Meshed up: Learnt error correction in 3D reconstructions. In *Proceedings of the IEEE International Conference on Robotics and Automation (*ICRA*)*, Brisbane, Australia.

Tomasi, C. and Manduchi, R. (1998). Bilateral filtering for gray and color images. In *Proceedings of the International Conference on Computer Vision (*ICCV*)*, pages 839–846.

Uhrig, J., Schneider, N., Schneider, L., Franke, U., Brox, T., and Geiger, A. (2017). Sparsity invariant CNNs. In *Proceedings of the IEEE International Conference on 3D Vision (*3DV*)*.

Ummenhofer, B., Zhou, H., Uhrig, J., Mayer, N., Ilg, E., Dosovitskiy, A., and Brox, T. (2017). DeMoN: Depth and motion network for learning monocular stereo. In *Proceedings of the IEEE International Conference on Computer Vision and Pattern Recognition (*CVPR*)*, pages 5622–5631.

Zhang, Y. and Funkhouser, T. A. (2018). Deep depth completion of a single RGB-D image. In *Proceedings of the IEEE International Conference on Computer Vision and Pattern Recognition (*CVPR*)*, pages 175–185.

Zhou, T., Brown, M., Snavely, N., and Lowe, D. G. (2017). Unsupervised learning of depth and ego-motion from video. In *Proceedings of the IEEE International Conference on Computer Vision and Pattern Recognition (*CVPR*)*.